Article

# Self-Assembled TiO–Graphene Hybrid Nanostructures for Enhanced Li-Ion Insertion

Donghai Wang, Daiwon Choi, Juan Li, Zhenguo Yang, Zimin Nie, Rong Kou, Dehong Hu, Chongmin Wang, Laxmikant V. Saraf, Jiguang Zhang, Ilhan A. Aksay, and Jun Liu

*ACS Nano*, **2009**, 3 (4), 907-914• DOI: 10.1021/nn900150y • Publication Date (Web): 26 March 2009



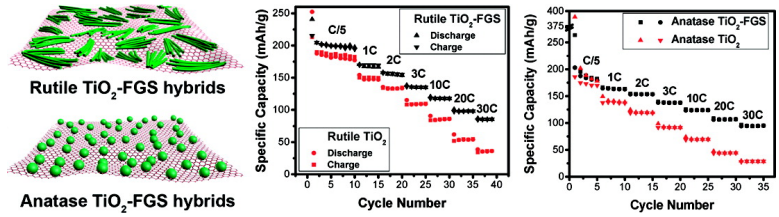


## More About This Article

Additional resources and features associated with this article are available within the HTML version:

- Supporting Information
- Access to high resolution figures
- Links to articles and content related to this article
- Copyright permission to reproduce figures and/or text from this article

View the Full Text HTML

# Self-Assembled $TiO_2$–Graphene Hybrid Nanostructures for Enhanced Li-Ion Insertion

**Donghai Wang,[†] Daiwon Choi,[†] Juan Li,[†] Zhenguo Yang,[†] Zimin Nie,[†] Rong Kou,[†] Dehong Hu,[†] Chongmin Wang,[†] Laxmikant V. Saraf,[†] Jiguang Zhang,[†] Ilhan A. Aksay,[‡,*] and Jun Liu[†,*]**

[†]Pacific Northwest National Laboratory Richland, Washington 99352 and [‡]Department of Chemical Engineering, Princeton University, Princeton, New Jersey 08544

**ABSTRACT** We used anionic sulfate surfactants to assist the stabilization of graphene in aqueous solutions and facilitate the self-assembly of in situ grown nanocrystalline $TiO_2$, rutile and anatase, with graphene. These nanostructured $TiO_2$-graphene hybrid materials were used for investigation of Li-ion insertion properties. The hybrid materials showed significantly enhanced Li-ion insertion/extraction in $TiO_2$. The specific capacity was more than doubled at high charge rates, as compared with the pure $TiO_2$ phase. The improved capacity at high charge—discharge rate may be attributed to increased electrode conductivity in the presence of a percolated graphene network embedded into the metal oxide electrodes.

**KEYWORDS:** graphene · metal oxide · hybrid nanostructure · Li-ion · battery

Electrochemical energy storage has been receiving great attention for potential applications in electric vehicles and renewable energy systems from intermittent wind and solar sources. Currently, Li-ion batteries are being considered as the leading candidates for hybrid, plug-in hybrid, and all electrical vehicles, and possibly for utility applications as well. However, many potential electrode materials (*e.g.*, oxide materials) in Li-ion batteries are limited by slow Li-ion diffusion, poor electron transport in electrodes, and increased resistance at the interface of electrode/electrolyte at high charge—discharge rates.[1,2] To improve the charge—discharge rate performance of Li-ion batteries, extensive work has focused on improving Li-ion and/or electron transport in electrodes.[3] The use of nanostructures (*e.g.*, nanoscale size or nanoporous structure) has been widely investigated to improve the Li-ion transport in electrode by shortening the Li-ion insertion/extraction pathway.[3,4] In addition, a variety of approaches have also been developed to increase electron transport in the electrode materials, such as conductive coating (*e.g.*, carbon[5−7]), and uses of conductive additives (*e.g.*, conductive oxide wires or networks,[8,9] and conductive polymers[10,11]). Recently, $TiO_2$ has been extensively studied to demonstrate the effectiveness of nanostructure and conductive coating.[12−21] $TiO_2$ is studied because it is an abundant, low cost, and environmentally benign material. $TiO_2$ is also structurally stable during Li-insertion/extraction and is intrinsically safe by avoiding Li electrochemical deposition. These properties make $TiO_2$ particularly attractive for large scale energy storage.

Another way to improve the Li-ion insertion properties is to introduce hybrid nanostructured electrodes that interconnect nanostructured electrode materials with conductive additive nanophases. For example, hybrid nanostructures, such as $V_2O_5$-carbon nanotube (CNT) or anatase $TiO_2$—CNT hybrids, $LiFePO_4$—$RuO_2$ nanocomposite, and anatase $TiO_2$—$RuO_2$ nanocomposite,[22−25] combined with conventional carbon additives (*e.g.*, Super P carbon or acetylene black), have demonstrated an increased Li-ion insertion/extraction capacity in the hybrid electrodes at high charge/discharge rates. While the hybrids or nanocomposites offer significant advantages, some of the candidate materials to improve the conductivity, such as $RuO_2$ and CNTs,[24,25] are inherently expensive. In addition, conventional carbon additives at high loading content (20 wt % or more) are still needed to ensure good electron transport in fabricated electrodes.[24,25] To improve high-rate performance and reduce cost of the electrochemically active materials, it is important to identify high surface area, inexpensive, and highly conductive nanostructured materials that can be integrated with electrochemical active materials at nanoscale.

Graphene as a two-dimensional macromolecular sheet of carbon atoms with a honeycomb structure has excellent

*Address correspondence to jun.liu@pnl.gov, iaksay@princeton.edu.

Received for review February 13, 2009 and accepted March 11, 2009.

**Published online March 26, 2009.**
10.1021/nn900150y CCC: $40.75

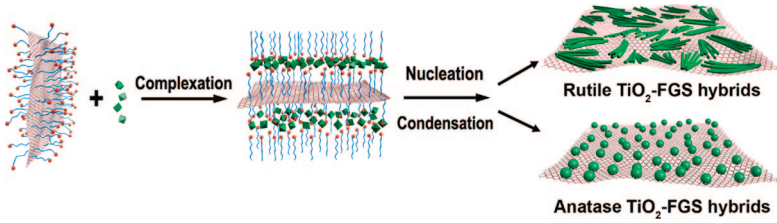


**Scheme 1. Anionic Sulfate Surfactant Mediated Stabilization of Graphene and Growth of Self-Assembled $TiO_2$—FGS Hybrid Nanostructures**

electronic conductivity and mechanical properties,[26−29] and may be the ideal conductive additive for hybrid nanostructured electrodes. Other advantages of graphene include high surface area (theoretical value of 2630 $m^2/g$)[30] for improved interfacial contact and potential for low manufacturing cost as compared to CNTs, especially when it is produced as functionalized graphene sheets through the thermal expansion of graphite oxide.[31,32] Recently, high-surface-area graphene sheets have been studied for direct Li-ion storage by expanding the layer spacing between the graphene sheets.[33] In addition, graphene has been used to form composite materials with $SnO_2$ for improving capacity and cyclic stability of the anode materials.[34]

In this paper, we demonstrate the use of graphene as a conductive additive in self-assembled hybrid nanostructures to enhance high rate performance of electrochemical active materials. We choose metal oxide $TiO_2$ as a model electrochemical active oxide material, but this method can be applied to other materials as well. Several methods have been reported to synthesize metal oxide—graphene nanocomposites (*e.g.*, with $TiO_2$, $Al_2O_3$, $SnO_2$, and clay).[34−37] For example, $TiO_2$ particles and graphene oxide colloids have been mixed ultrasonically followed by the reduction of graphene oxide to yield $TiO_2$—graphene nanocomposites.[35] Preformed $SnO_2$ nanoparticles have been chemically mixed with graphene to form composite materials.[34] Here we report a one-step synthesis approach to prepare metal oxide—graphene hybrid nanostructures. In our system, the reduced and highly conductive form of graphene is hydrophobic and oxides are hydrophilic. To ensure uniform coating of the metal oxide on graphene surfaces, we use an approach akin to the pioneering studies done with atomic force microscopy (AFM) on the self-assembly of surfactant micelles and their hybrid nanostructures with inorganics on highly oriented pyrolytic graphite.[38,39] The use of surfactants not only solves the hydrophobic/hydrophilic incompatibility problem, but also provides the molecular template for controlled nucleation and growth of the nanostructured inorganics.[38,40] This approach, schematically illustrated in Scheme 1, starts with the dispersion of the graphene sheets with an anionic sulfate surfactant (*i.e.*, sodium dodecyl sulfate) and proceeds with the self-assembly of surfactants with the metal oxide precursor and the *in situ* crystallization of metal oxide precursors to produce the desired oxide phase and morphology.

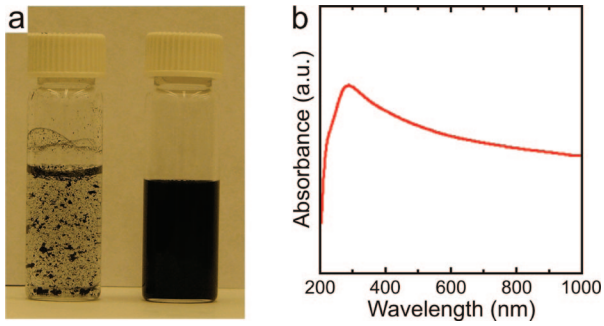


**Figure 1. (a) A photograph of FGSs (left) and SDS-FGS aqueous dispersion (right); (b) UV—vis absorbance of the SDS-FGS aqueous dispersion.**

## RESULTS AND DISCUSSION

**Self-Assembly of Metal Oxides and Functionalized Graphene Sheets.** Functionalized graphene sheets (FGSs) used in this study were prepared through the thermal expansion of graphite oxide.[31,32] In comparison to the graphene produced by the chemical reduction of graphene oxide,[41,42] graphene prepared by the thermal expansion approach can have tunable C/O ratios ranging from 10 to 500 and thus its conductivity can be tuned to higher values. FGSs processing starts with chemical oxidation of graphite flakes to increase the *c*-axis spacing from 0.34 to 0.7 nm as described elsewhere.[31,32] The resultant graphite oxide is then split by a rapid thermal expansion to yield separated graphene sheets. X-ray photoemission spectroscopy (XPS) of FGSs shows a sharp C1s peak indicating good $sp^2$ conjugation (Figure S1 in Supporting Information (SI)). A small shoulder at 286 eV indicates the existence of some C—O bonds corresponding to the epoxy and hydroxyl functional groups on FGSs. Sodium dodecyl

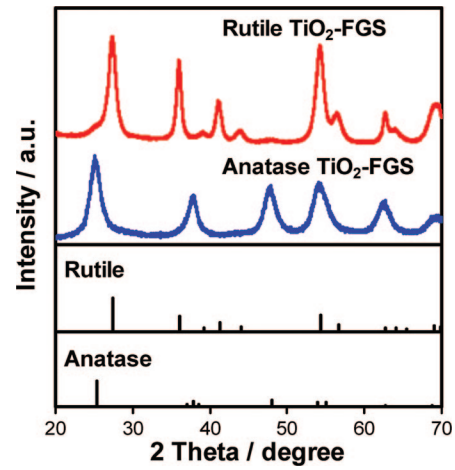


**Figure 2. XRD patterns of anatase $TiO_2$—FGS and rutile $TiO_2$—FGS hybrid materials. Standard diffraction peaks of anatase $TiO_2$ (JCPDS No. 21-1272) and rutile $TiO_2$ (JCPDS No. 21-1276) are shown as vertical bars.**

sulfate (SDS)-FGS aqueous dispersions were prepared by ultrasonication. Similar to the colloidal stabilization of CNTs using SDS,[43,44] the SDS-FGS aqueous dispersions were stable. Only minor sedimentation was observed after a week at room temperature (Figure 1a). UV−vis spectrum of the SDS-FGS dispersion showed an absorption peak at 275 nm with a broad absorption background (Figure 1b) that is consistent with that of aqueous stable graphene sheets.[45] Raman spectra of FGSs and calcined $TiO_2$−FGS showed similar G and D bands structure of carbon, indicating that the structure of graphene is maintained during the synthesis procedure (Figure S2 in SI).

A mild, low-temperature (below 100 °C) crystallization process was carried out to form crystalline $TiO_2$ with controlled crystalline phase (*i.e.*, rutile and anatase) on the graphene sheets (see Methods).[46,47] The low temperature condition was also important in preventing aggregation of graphene sheets at elevated temperatures.[48] Consistent with our previous studies by the low-temperature oxidative hydrolysis and crystallization, rutile $TiO_2$−FGS is obtained with a minor anatase phase. To obtain anatase $TiO_2$−FGS, additional sodium sulfate was added to the solution to promote the formation of anatase phase.[49] The XRD patterns (Figure 2) of the $TiO_2$−FGS hybrids show the formation of nanocrystalline rutile and anatase metal oxides with an estimated crystalline domain size of 6 and 5 nm, respectively.

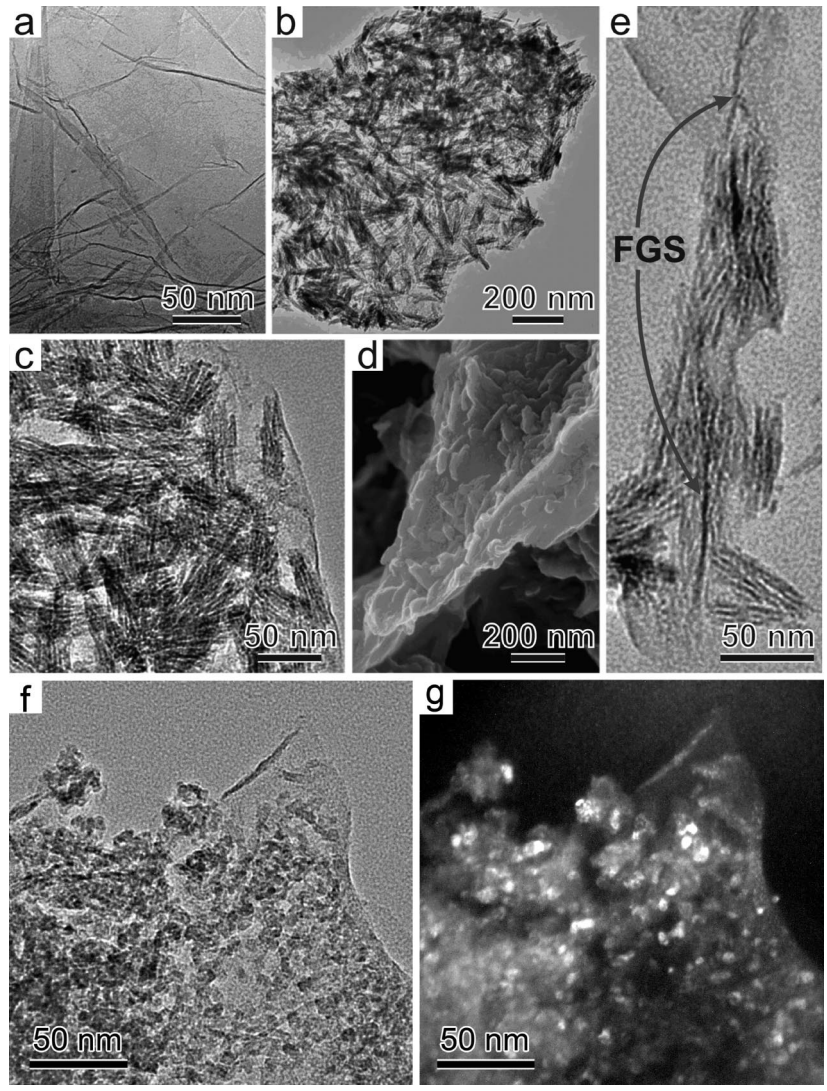


**Figure 3. (a) TEM image of FGSs. (b, c, and d) Low- and high-magnification TEM and SEM images of the self-assembled rutile $TiO_2$−FGS hybrids, respectively. (e) Cross-section TEM image of rutile $TiO_2$−FGS hybrid showing nanostructured rutile $TiO_2$ lying on the FGS. (f) Plane-view TEM image of anatase $TiO_2$−FGS hybrid nanostructures. (g) Dark-field TEM image of the antase $TiO_2$−FGS hybrid nanostructure.**

**Characterization of Hybrid Nanostructures.** Typical morphology of FGSs is shown in the transmission electron microscopy (TEM) image of Figure 3a. The free-standing 2D FGSs are not perfectly flat but display intrinsic microscopic roughening and out-of-plane deformations (wrinkles). More than 80% of the FGSs has been shown to be single sheets by AFM characterization,[31] when they were deposited onto an atomically smooth, highly oriented pyrolytic carbon (HOPG) template. Some regions appeared as multilayers in the TEM images, which may represent the parts that either have not been fully split apart or the parts that have restacked together due to capillary and the van der Waals forces during the drying process.[31]

Figure 3panels b−e show TEM and scanning electron microscopy (SEM) images of as-grown rutile $TiO_2$−FGS hybrid nanostructures. Figure 3 panels b and c show planar views of FGSs covered with nanostructured $TiO_2$. Both the edge of graphene and the nanostructure of the $TiO_2$ are clearly observable in the higher magnification image of Figure 3c. The nanostructured $TiO_2$ is composed of rodlike rutile nanocrystals organized in parallel interspaced with the SDS surfactants, which is consistent with our previous studies in the formation of mesoporous rutile.[47] The SEM image of Figure 3d shows randomly oriented rod-like nanostructured rutile lying on the FGSs. The cross-section TEM image further confirms that the nanostructured rutile mostly lies on the FGSs with the rod length parallel to the graphene surface (Figure 3e). Figure 3 panels f and g show plane-view TEM images of anatase $TiO_2$−FGS hybrid nanostructures. FGSs underneath are covered with spherical aggregated anatase $TiO_2$ nanoparticles. The dark-field TEM image (Figure 3g) further confirms crystalline $TiO_2$ nanoparticles (bright spot) with a diameter of 5 nm spreading over the graphene surface.

It is important to note that the SDS surfactant determines the interfacial interactions between graphene and the oxide materials in promoting the formation of

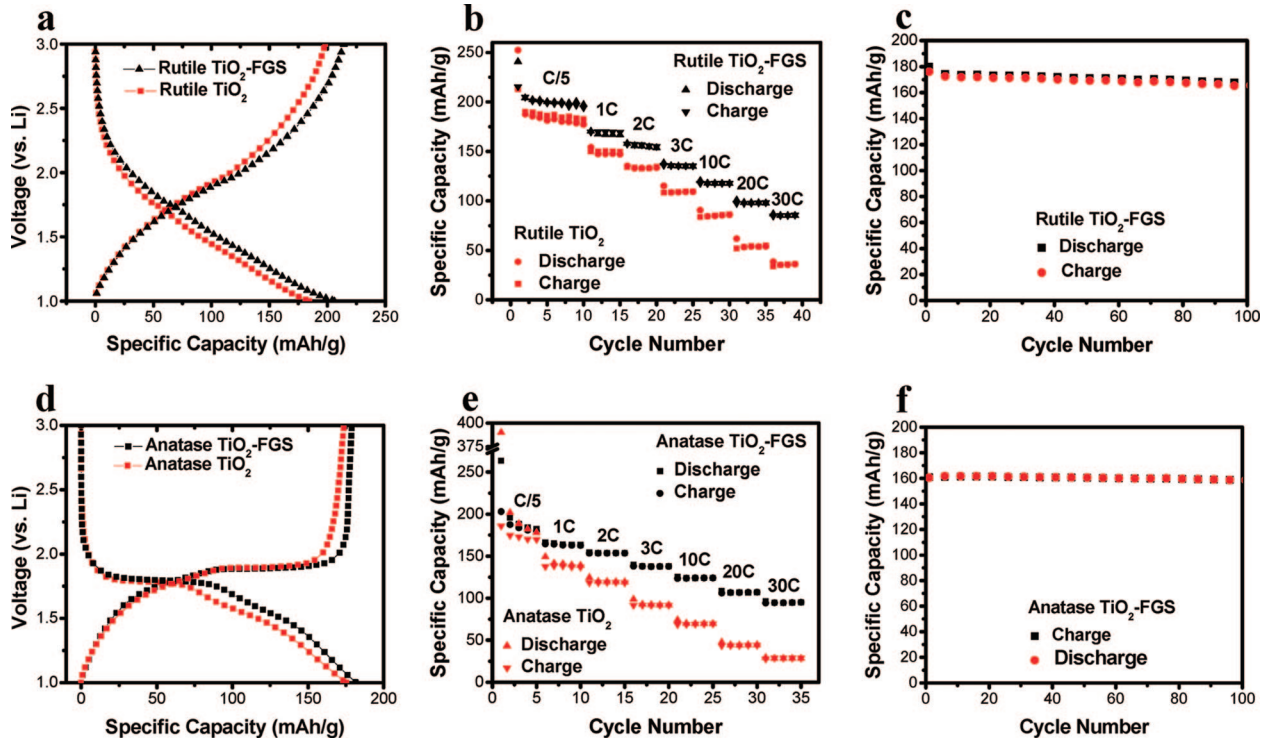


**Figure 4. (a) Charge−discharge profiles for control rutile $TiO_2$ and rutile $TiO_2$−FGS (0.5 wt % FGSs) hybrid nanostructures at C/5 charge−discharge rates. (b) Specific capacity of control rutile $TiO_2$ and the rutile $TiO_2$−FGS hybrids at different charge/discharge rates. (c) Cycling performance of the rutile $TiO_2$−FGS up to 100 cycles at 1C charge/discharge rates after testing at various rates shown in Figure 4b. (d) Charge−discharge profiles for control anatase $TiO_2$ and anatase $TiO_2$−FGS (2.5 wt % FGSs) hybrid nanostructures at C/5 charge−discharge rates. (e) Specific capacity of control anatase $TiO_2$ and the anatase $TiO_2$−FGS hybrids at different charge/discharge rates. (f) Cycling performance of the anatase $TiO_2$−FGS up to 100 cycles at 1C charge/discharge rates after testing at various rates shown in Figure 4e.**

$TiO_2$-hybrid nanostructures. When the surfactant molecules are added, they can adsorb onto graphene through the hydrophobic tails[39] making FGSs highly dispersed and interact with the oxide precursor through the hydrophilic head groups. The cooperative interactions between the surfactant, the graphene, and the oxide precursors lead to the homogeneous mixing of the components, in which the hydrophobic graphene most likely resides in the hydrophobic domains of the SDS micelles. As nanocrystalline $TiO_2$ formed, as-grown nanoparticles are then coated to the graphene surfaces since sulfate head groups have strong bonding with $TiO_2$.[50] Without the surfactant, some of the surface functional sites (*e.g.*, carboxylate, epoxy, and hydroxyl groups) on FGSs may provide bonding to $TiO_2$ nanoparticles. However, only a very small amount of the metal oxides will then be attached to graphene through such interactions because of the low number density of these functional groups on FGSs. Thus, in the control samples without the surfactant, FGSs are barely covered with the metal oxides (Figure S3 in SI) along with phase separation from $TiO_2$. This indicates the important role of SDS in the formation of the self-assembled hybrid nanostructures.

**Li-Ion Insertion/Extraction in Hybrid Nanostructures.** To examine the effectiveness of FGSs in improving the rate capability of the electrode, we investigated the Li-ion insertion/extraction properties in the $TiO_2$−FGS hybrid materials. The electrodes were fabricated in a conventional way by mixing the hybrid materials with Super P carbon additive and a PVDF binder and thus tested in Li-ion battery coin cell (see Methods). The rutile $TiO_2$−FGS hybrid showed a slope profile of voltage-capacity relationship at both the charge and discharge state (Figure 4a), similar to that of control rutile $TiO_2$ and nanostructured rutile studied previously.[17] As shown in Figure 4b, with the incorporation of FGSs, specific capacity of rutile $TiO_2$ in the hybrids (0.5 wt % FGSs) increased at all charge/discharge rates compared with the control rutile $TiO_2$. The relative increase in specific capacity is especially larger at higher rates. For instance, at a rate of 30C (2 min of charging or discharging), the specific capacity of the rutile $TiO_2$−FGS hybrid material is 87 mAh/g which is more than double the high rate capacity (35 mAh/g) of the control rutile $TiO_2$ (Figure 4b).

Voltage-capacity profile of anatase $TiO_2$−FGS (2.5 wt % FGSs) at C/5 rate shows plateaus around 1.8 V (discharge process) and 1.9 V (charge process) in Figure 4d, which is similar to that of control anatase $TiO_2$ and nanostructured anatase.[25] The plateaus are related to the phase transition between the tetragonal and orthorhombic phases with Li insertion into anatase $TiO_2$. Similar to rutile $TiO_2$−FGS, specific capacity of the anatase $TiO_2$−FGS hybrid is enhanced at all

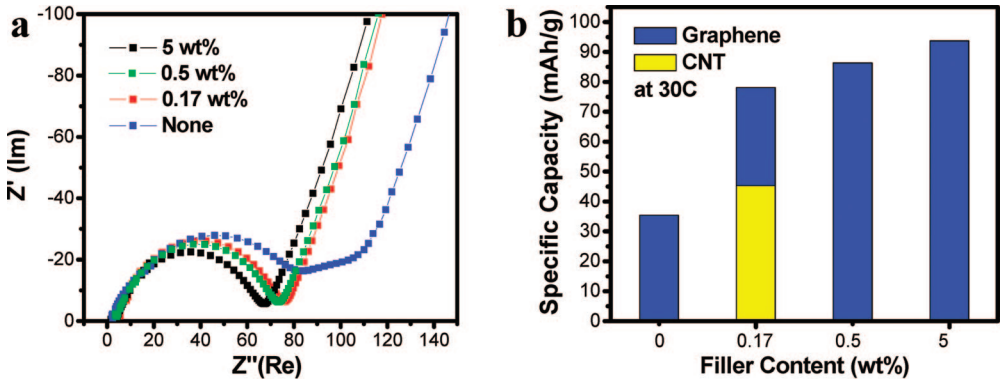


**Figure 5. (a) Impedance measurement of coin cells using the electrode materials of control rutile $TiO_2$ and rutile $TiO_2$−FGS hybrids with different weight percentage of FGSs. (b) Specific capacity of rutile $TiO_2$−CNT and rutile $TiO_2$−FGS at 30C rate with different percentage of graphene.**

charge−discharge rates (Figure 4e). The specific capacity of the anatase $TiO_2$−FGS at the rate of 30C is as high as 96 mAh/g compared with 25 mAh/g of control anatase $TiO_2$. Furthermore, the Coulombic efficiencies of $TiO_2$−FGS hybrids at various charge/discharge rates are greater than 98% (Figure S4 in SI). Both rutile and anatase $TiO_2$−FGS hybrids show good capacity retention of the Li-ion insertion/extraction over 100 cycles at 1C rate, as shown in Figure 4c and 4f.

To identify the capacity contribution from FGSs, Li-ion insertion/extraction behavior of the FGSs was also studied. The initial capacity of FGSs of 100 mAh/g with 50% irreversible loss is observed between 1∼3 V potential window applied, which is consistent with a recent study of Li-ion storage in graphene.[33] However, the specific capacity of FGSs rapidly decreases to 25 mAh/g within 10 cycles. At higher charge/discharge rates, the capacity of FGSs has almost negligible Li-ion insertion (Figure S5 in SI). For 1 wt % FGSs hybrids, capacity contribution from FGSs itself after 2 cycles can be a maximum value of 0.4 mAh/g. Thus, the increase of the specific capacity at high rate is not attributed to the capacity of the graphene additive itself in the hybrid materials.

To further understand the improved high-rate performance, electrochemical impedance spectroscopy measurements on rutile $TiO_2$−FGS hybrid materials were performed after cycles. The Nyquist plots of the rutile $TiO_2$−FGS electrode materials with different percentage of graphene cycled in electrolyte (Figure 5a) all show depressed semicycles at high frequencies. As electrolyte and electrode fabrication are similar between each electrode, the high frequency semicircle should relate to the resistance of electrode. We estimate that the resistivity of the cells decreased from 93 Ω for the pure $TiO_2$ to 73 Ω with the addition of only 0.5 wt % graphene. Therefore, improved high charge rate performance may be attributed to the increased conductivity of the hybrid materials, but the synergistic effect on electron and Li ion transport needs to be more carefully studied.

By increasing the graphene percentage in the hybrid materials further, the specific capacity is slightly increased, e.g., to 93 mAh/g in the hybrid material with 5 wt % FGSs, indicating that a kinetic capacity limitation may be reached by only improving the electrode conductivity with the incorporation of FGSs (Figure 5b). Rutile $TiO_2$−CNT hybrids prepared and tested under similar conditions showed less increase in specific capacity (yellow bar in Figure 5b). Similarly, hybrid nanostructures prepared using solution reduced graphene oxides also showed even less improved performance, indicating the importance of the highly conducting graphene phase of FGSs.

To study the properties of electrode materials without any Super P carbon, we also compared Li-ion insertion/extraction properties of the rutile $TiO_2$−FGS (10 wt % graphene) and control rutile $TiO_2$ with 10 wt % Super P at high charge−discharge rates. The hybrid material showed a much higher capacity at all charge−discharge rates, as shown in Figure 6. This result indeed confirms that the graphene in the self-

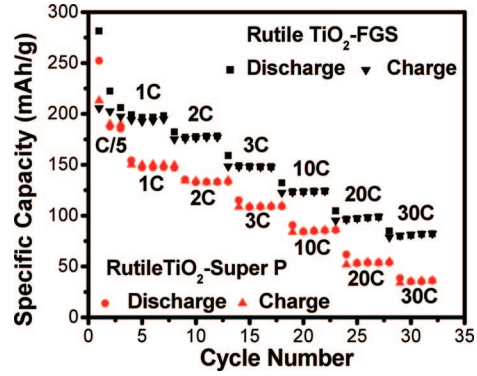


**Figure 6. Specific capacity of control rutile $TiO_2$ (10 wt % Super P) and rutile $TiO_2$−FGS hybrids (10 wt % FGSs) at different charge/discharge rates. Rutile $TiO_2$−FGS hybrid electrode was prepared by mixing the calcined hybrid with PVDF binder at a mass ratio of 90:10. Control $TiO_2$ electrode was prepared by mixing the hybrid, Super P and PVDF binder at a mass ratio of 80:10:10.**

assembled hybrid materials is more effective than the commonly used Super P carbon materials in improving high rate performance of the electrode materials.

The high rate performance is important for applications where fast charge and discharge is needed, such as in load leveling utility applications. The high rate properties obtained from the graphene nanocomposite materials are comparable to some of the best results reported in the literature using $RuO_2$ or carbon nanotubes with a higher carbon (Super P) additive content.[24,25] The simple self-assembly approach, and the potential low manufacturing cost of graphene may provide a new pathway for large scale applications of novel hybrid nanocomposite materials for energy storage.

## CONCLUSIONS

In summary, we developed an anionic surfactant mediated growth of self-assembled metal oxide−graphene hybrid nanostructures. The nanostructured $TiO_2$−graphene hybrid materials show enhanced Li-ion insertion/extraction kinetics in $TiO_2$, especially at high charge/discharge rates. This demonstrates that functionalized graphene sheets are a promising conductive additive for Li-ion battery electrode materials. Although our current studies only present results on rutile and anatase $TiO_2$−graphene hybrid systems, we expect that the self-assembly approach discussed here can be applied to other metal oxide-graphene hybrid nanostructures to study synergetic properties and improve the performance of oxide electrodes in electrochemical energy storage and conversion.

## METHODS

**Synthesis Procedures.** In a typical preparation of rutile $TiO_2$−FGS hybrid materials (*e.g.*, 0.5 wt % FGSs), 2.4 mg of FGSs and 3 mL of SDS aqueous solution (0.5 mol/L) were mixed together. The mixture was diluted to 15 mL and sonicated for 10−15 min (Branson Sonifer S-450A, 400 W). A 25 mL portion of $TiCl_3$ (0.12 mol/L) aqueous solution was added into as-prepared SDS−FGS dispersions while stirring. Then, 2.5 mL of $H_2O_2$ (1 wt %) was added dropwise followed by deionized water under vigorous stirring until reaching a total volume of 80 mL. Similarly, 0.8, 26.4, and 60 mg of FGSs were used to prepare the hybrid materials with 0.17, 5, and 10 wt % FGSs, respectively. Rutile $TiO_2$−CNT (0.5 wt % carbon nanotubes) hybrid materials were prepared using corresponding single-wall CNTs (2.4 mg) according to the above method. In a typical preparation of anatase $TiO_2$−FGS hybrid materials (*e.g.*, 2.5 wt % FGSs), 13 mg of FGSs, and 0.6 mL of SDS aqueous solution (0.5 mol/L) were mixed and sonicated to prepare an SDS−FGS dispersion. A 25 mL portion of $TiCl_3$ (0.12 mol/L) aqueous solution was added into as-prepared SDS−FGS dispersions while stirring, followed by the addition of 5 mL of 0.6 M $Na_2SO_4$; 2.5 mL of $H_2O_2$ (1 wt %) was then added dropwise followed by addition of deionized water under vigorous stirring until reaching a total volume of 80 mL.

All of these resulting mixtures were further stirred in a sealed polypropylene flask at 90 °C for 16 h. The precipitates were separated by centrifuge followed by washing with deionized water and ethanol. The centrifuging and washing processes were repeated three times. The product was then dried in a vacuum oven at 70 °C overnight and subsequently calcined in static air at 400 °C for 2 h. The thermal gravimetric analysis (TGA) indicated approximately 50 wt % percentage loss of FGSs during calcination in air at 400 °C for 2 h (Figure S6 in SI). Weigh percentage of graphene in the hybrid materials is correspondingly normalized, which is consistent with TGA of the hybrid materials.

**Characterization.** XRD patterns were obtained on a Philips Xpert X-ray diffractometer using Cu Kα radiation at $\lambda = 1.54$ Å. The TEM imaging was performed on a JEOL JSM-2010 TEM operated at 200 kV. SEM images were obtained on an FEI Helios Nanolab dual-beam focused ion beam/scanning electron microscope (FIB/SEM) operated at 2 kV. XPS characterization was performed using a Physical Electronics Quantum 2000 scanning ESCA microprobe with a focused monochromatic Al Kα X-ray (1486.7 eV) source and a spherical section analyzer. Electrochemical experiments were performed with coin cells (type 2335, half-cell) using Li foil as counter-electrode. The working electrode was prepared using the mixture of calcined $TiO_2$−FGS or control $TiO_2$, Super P and poly (vinylidene fluoride) (PVDF) binder dispersed in *N*-methylpyrrolidone (NMP) solution. For the preparation of rutile $TiO_2$ electrode (less than 5 wt % graphene), the mass ratio of rutile $TiO_2$−hybrid or control rutile $TiO_2$, Super P, and PVDF was 80:10:10. For the preparation of anatase $TiO_2$ electrode, the mass ratio was 70:20:10 and 80:10:10 for control anatase $TiO_2$ and anatase $TiO_2$−FGS hybrid (2.5 wt% FGSs), respectively. Rutile $TiO_2$−FGS hybrid (10 wt % FGSs) electrode was prepared with a mass ratio of hybrid and PVDF binder at 90:10 without Super P. The resultant slurry was then uniformly coated on an aluminum foil current collector and dried overnight in air. The electrolyte used was 1 M $LiPF_6$ dissolved in the mixture of ethyl carbonate (EC) and dimethyl carbonate (DMC) with the volume ratio of 1:1. The coin cells were assembled in an argon-filled glovebox. The electrochemical performance of $TiO_2$−graphene was characterized with an Arbin battery testing system at room temperature. The electrochemical tests were performed between 3∼1 V *vs* $Li^+$/Li and C-rate currents applied were calculated based on rutile $TiO_2$ theoretical capacity of 168 mAh/g.

*Acknowledgment.* The work is supported by Laboratory-Directed Research and Development Program (LDRD) of the Pacific Northwest National Laboratory (PNNL) and by the Office of Basic Energy Sciences (BES), U.S. Department of Energy (DOE). TEM investigation was performed in the EMSL, a national scientific user facility sponsored by the Department of Energy's Office of Biological and Environmental Research and located at Pacific Northwest National Laboratory. PNNL is a multiprogram laboratory operated by Battelle Memorial Institute for the Department of Energy under Contract DE-AC05-76RL01830. IAA acknowledges support from DARPA and ARO/MURI under grant number W911NF-04-1-0170. We thank Michael C. Perkins for the graphics.

*Supporting Information Available:* XPS, Li-ion insertion/extraction cycling capacity, TGA of functionalized graphene sheets, and XRD, Raman, and SEM of $TiO_2$−FGS. This material is available free of charge *via* the Internet at http://pubs.acs.org.

## REFERENCES AND NOTES

1. Maier, J. Nanoionics: Ion Transport and Electrochemical Storage in Confined Systems. *Nat. Mater.* **2005**, *4*, 805–815.
2. Tarascon, J. M.; Armand, M. Issues and Challenges Facing Rechargeable Lithium Batteries. *Nature* **2001**, *414*, 359–367.
3. Arico, A. S.; Bruce, P.; Scrosati, B.; Tarascon, J. M.; Van Schalkwijk, W. Nanostructured Materials for Advanced Energy Conversion and Storage Devices. *Nat. Mater.* **2005**, *4*, 366–377.
4. Sakamoto, J. S.; Dunn, B. Hierarchical Battery Electrodes Based on Inverted Opal Structures. *J. Mater. Chem.* **2002**, *12*, 2859–2861.

5. Chen, Z. H.; Dahn, J. R. Reducing Carbon in $LiFePO_4$/C Composite Electrodes to Maximize Specific Energy, Volumetric Energy, and Tap Density. *J. Electrochem. Soc.* **2002**, *149*, A1184−A1189.
6. Prosini, P. P.; Zane, D.; Pasquali, M. Improved Electrochemical Performance of a $LiFePO_4$-Based Composite Cathode. *Electrochim. Acta* **2001**, *46*, 3517–3523.
7. Dominko, R.; Bele, M.; Gaberscek, M.; Remskar, M.; Hanzel, D.; Pejovnik, S.; Jamnik, J. Impact of the Carbon Coating Thickness on the Electrochemical Performance of $LiFePO_4$/C Composites. *J. Electrochem. Soc.* **2005**, *152*, A607−A610.
8. Erjavec, B.; Dominko, R.; Umek, P.; Sturm, S.; Pejovnik, S.; Gaberscek, M.; Jamnik, J. $RuO_2$-Wired High-Rate Nanoparticulate $TiO_2$ (Anatase): Suppression of Particle Growth Using Silica. *Electrochem. Commun.* **2008**, *10*, 926–929.
9. Herle, P. S.; Ellis, B.; Coombs, N.; Nazar, L. F. Nano-Network Electronic Conduction in Iron and Nickel Olivine Phosphates. *Nat. Mater.* **2004**, *3*, 147–152.
10. Leroux, F.; Koene, B. E.; Nazar, L. F. Electrochemical Lithium Intercalation into a Polyaniline/$V_2O_5$ Nanocomposite. *J. Electrochem. Soc.* **1996**, *143*, L181−L183.
11. Goward, G. R.; Leroux, F.; Nazar, L. F. Poly(Pyrrole) and Poly(Thiophene)/Vanadium Oxide Interleaved Nanocomposites: Positive Electrodes for Lithium Batteries. *Electrochim. Acta* **1998**, *43*, 1307–1313.
12. Armstrong, G.; Armstrong, A. R.; Bruce, P. G.; Reale, P.; Scrosati, B. $TiO_2$(B) Nanowires as an Improved Anode Material for Lithium-Ion Batteries Containing $LiFePO_4$ or $LiNi_{0.5}Mn_{1.5}O_4$ Cathodes and a Polymer Electrolyte. *Adv. Mater.* **2006**, *18*, 2597–2600.
13. Kavan, L.; Gratzel, M.; Rathousky, J.; Zukal, A. Nanocrystalline $TiO_2$(Anatase) Electrodes: Surface Morphology, Adsorption, and Electrochemical Properties. *J. Electrochem. Soc.* **1996**, *143*, 394–400.
14. Armstrong, A. R.; Armstrong, G.; Canales, J.; Bruce, P. G. $TiO_2$-B Nanowires. *Angew. Chem., Int. Ed.* **2004**, *43*, 2286–2288.
15. Zukalova, M.; Kalbac, M.; Kavan, L.; Exnar, I.; Gratzel, M. Pseudocapacitive Lithium Storage in $TiO_2$ (B). *Chem. Mater.* **2005**, *17*, 1248–1255.
16. Zhou, Y. K.; Cao, L.; Zhang, F. B.; He, B. L.; Li, H. L. Lithium Insertion into $TiO_2$ Nanotube Prepared by the Hydrothermal Process. *J. Electrochem. Soc.* **2003**, *150*, A1246−A1249.
17. Hu, Y. S.; Kienle, L.; Guo, Y. G.; Maier, J. High Lithium Electroactivity of Nanometer-Sized Rutile $TiO_2$. *Adv. Mater.* **2006**, *18*, 1421–1426.
18. Baudrin, E.; Cassaignon, S.; Koesch, M.; Jolivet, J. P.; Dupont, L.; Tarascon, J. M. Structural Evolution During the Reaction of Li with Nano-Sized Rutile Type $TiO_2$ at Room Temperature. *Electrochem. Commun.* **2007**, *9*, 337–342.
19. Jiang, C. H.; Honma, I.; Kudo, T.; Zhou, H. S. Nanocrystalline Rutile $TiO_2$ Electrode for High-Capacity and High-Rate Lithium Storage. *Electrochem. Solid-State Lett.* **2007**, *10*, A127−A129.
20. Reddy, M. A.; Kishore, M. S.; Pralong, V.; Caignaert, V.; Varadaraju, U. V.; Raveau, B. Room Temperature Synthesis and Li Insertion into Nanocrystalline Rutile $TiO_2$. *Electrochem. Commun.* **2006**, *8*, 1299–1303.
21. Moskon, J.; Dominko, R.; Gaberscek, M.; Cerc-Korosec, R.; Jamnik, J. Citrate-Derived Carbon Nanocoatings for Poorly Conducting Cathode—A Detailed Study Using $TiO_2$ Substrate Materials. *J. Electrochem. Soc.* **2006**, *153*, A1805−A1811.
22. Sakamoto, J. S.; Dunn, B. Vanadium Oxide-Carbon Nanotube Composite Electrodes for Use in Secondary Lithium Batteries. *J. Electrochem. Soc.* **2002**, *149*, A26−A30.
23. Hu, Y. S.; Guo, Y. G.; Dominko, R.; Gaberscek, M.; Jamnik, J.; Maier, J. Improved Electrode Performance of Porous $LiFePO_4$ Using $RuO_2$ as an Oxidic Nanoscale Interconnect. *Adv. Mater.* **2007**, *19*, 1963–1966.
24. Guo, Y. G.; Hu, Y. S.; Sigle, W.; Maier, J. Superior Electrode Performance of Nanostructured Mesoporous $TiO_2$ (Anatase) through Efficient Hierarchical Mixed Conducting Networks. *Adv. Mater.* **2007**, *19*, 2087–2091.
25. Moriguchi, I.; Hidaka, R.; Yamada, H.; Kudo, T.; Murakami, H.; Nakashima, N. A Mesoporous Nanocomposite of $TiO_2$ and Carbon Nanotubes as a High-Rate Li-Intercalation Electrode Material. *Adv. Mater.* **2006**, *18*, 69–73.
26. Berger, C.; Song, Z. M.; Li, X. B.; Wu, X. S.; Brown, N.; Naud, C.; Mayo, D.; Li, T. B.; Hass, J.; Marchenkov, A. N.; Conrad, E. H.; First, P. N.; de Heer, W. A. Electronic Confinement and Coherence in Patterned Epitaxial Graphene. *Science* **2006**, *312*, 1191–1196.
27. Novoselov, K. S.; Geim, A. K.; Morozov, S. V.; Jiang, D.; Zhang, Y.; Dubonos, S. V.; Grigorieva, I. V.; Firsov, A. A. Electric Field Effect in Atomically Thin Carbon Films. *Science* **2004**, *306*, 666–669.
28. Stankovich, S.; Dikin, D. A.; Dommett, G. H. B.; Kohlhaas, K. M.; Zimney, E. J.; Stach, E. A.; Piner, R. D.; Nguyen, S. T.; Ruoff, R. S. Graphene-Based Composite Materials. *Nature* **2006**, *442*, 282–286.
29. Ramanathan, T.; Abdala, A. A.; Stankovich, S.; Dikin, D. A.; Herrera-Alonso, M.; Piner, R. D.; Adamson, D. H.; Schniepp, H. C.; Chen, X.; Ruoff, R. S.; Nguyen, S. T.; Aksay, I. A.; Prud'homme, R. K.; Brinson, L. C. Functionalized Graphene Sheets for Polymer Nanocomposites. *Nat. Nanotechnol.* **2008**, *3*, 327–331.
30. Peigney, A.; Laurent, C.; Flahaut, E.; Bacsa, R. R.; Rousset, A. Specific Surface Area of Carbon Nanotubes and Bundles of Carbon Nanotubes. *Carbon* **2001**, *39*, 507–514.
31. McAllister, M. J.; LiO, J. L.; Adamson, D. H.; Schniepp, H. C.; Abdala, A. A.; Liu, J.; Herrera-Alonso, M.; Milius, D. L.; CarO, R.; Prud'homme, R. K.; Aksay, I. A. Single Sheet Functionalized Graphene by Oxidation and Thermal Expansion of Graphite. *Chem. Mater.* **2007**, *19*, 4396–4404.
32. Schniepp, H. C.; Li, J. L.; McAllister, M. J.; Sai, H.; Herrera-Alonso, M.; Adamson, D. H.; Prud'homme, R. K.; Car, R.; Saville, D. A.; Aksay, I. A. Functionalized Single Graphene Sheets Derived from Splitting Graphite Oxide. *J. Phys. Chem. B* **2006**, *110*, 8535–8539.
33. Yoo, E.; Kim, J.; Hosono, E.; Zhou, H.-s.; Kudo, T.; Honma, I. Large Reversible Li Storage of Graphene Nanosheet Families for Use in Rechargeable Lithium Ion Batteries. *Nano Lett.* **2008**, *8*, 2277–2282.
34. Paek, S.-M.; Yoo, E.; Honma, I. Enhanced Cyclic Performance and Lithium Storage Capacity of $SnO_2$/Graphene Nanoporous Electrodes with Three-Dimensionally Delaminated Flexible Structure. *Nano Lett.* **2009**, *9*, 72–75.
35. Williams, G.; Seger, B.; Kamat, P. V. $TiO_2$-Graphene Nanocomposites. UV-Assisted Photocatalytic Reduction of Graphene Oxide. *ACS Nano* **2008**, *2*, 1487–1491.
36. Wang, X. R.; Tabakman, S. M.; Dai, H. J. Atomic Layer Deposition of Metal Oxides on Pristine and Functionalized Graphene. *J. Am. Chem. Soc.* **2008**, *130*, 8152–8153.
37. Nethravathi, C.; Rajamathi, J. T.; Ravishankar, N.; Shivakumara, C.; Rajamathi, M. Graphite Oxide-Intercalated Anionic Clay and Its Decomposition to Graphene−Inorganic Material Nanocomposites. *Langmuir* **2008**, *24*, 8240–8244.
38. Aksay, I. A.; Trau, M.; Manne, S.; Honma, I.; Yao, N.; Zhou, L.; Fenter, P.; Eisenberger, P. M.; Gruner, S. M. Biomimetic Pathways for Assembling Inorganic Thin Films. *Science* **1996**, *273*, 892–898.
39. Schniepp, H. C.; Saville, D. A.; Aksay, I. A. Self-Healing of Surfactant Surface Micelles on Millisecond Time Scales. *J. Am. Chem. Soc.* **2006**, *128*, 12378–12379.
40. Kresge, C. T.; Leonowicz, M. E.; Roth, W. J.; Vartuli, J. C.; Beck, J. S. Ordered Mesoporous Molecular-Sieves Synthesized by a Liquid-Crystal Template Mechanism. *Nature* **1992**, *359*, 710–712.
41. Gomez-Navarro, C.; Weitz, R. T.; Bittner, A. M.; Scolari, M.; Mews, A.; Burghard, M.; Kern, K. Electronic Transport Properties of Individual Chemically Reduced Graphene Oxide Sheets. *Nano Lett.* **2007**, *7*, 3499–3503.
42. Si, Y.; Samulski, E. T. Synthesis of Water Soluble Graphene. *Nano Lett.* **2008**, *8*, 1679–1682.

43. Bonard, J. M.; Stora, T.; Salvetat, J. P.; Maier, F.; Stockli, T.; Duschl, C.; Forro, L.; deHeer, W. A.; Chatelain, A. Purification and Size-Selection of Carbon Nanotubes. *Adv. Mater.* **1997**, *9*, 827–831.
44. Richard, C.; Balavoine, F.; Schultz, P.; Ebbesen, T. W.; Mioskowski, C. Supramolecular Self-Assembly of Lipid Derivatives on Carbon Nanotubes. *Science* **2003**, *300*, 775–778.
45. Li, D.; Muller, M. B.; Gilje, S.; Kaner, R. B.; Wallace, G. G. Processable Aqueous Dispersions of Graphene Nanosheets. *Nat. Nanotechnol.* **2008**, *3*, 101–105.
46. Wang, D. H.; Ma, Z.; Dai, S.; Liu, J.; Nie, Z. M.; Engelhard, M. H.; Huo, Q. S.; Wang, C. M.; Kou, R. Low-Temperature Synthesis of Tunable Mesoporous Crystalline Transition Metal Oxides and Applications as Au Catalyst Supports. *J. Phys. Chem. C* **2008**, *112*, 13499–13509.
47. Wang, D. H.; Choi, D. W.; Yang, Z. G.; Viswanathan, V. V.; Nie, Z. M.; Wang, C. M.; Song, Y. J.; Zhang, J. G.; Liu, J. Synthesis and Li-Ion Insertion Properties of Highly Crystalline Mesoporous Rutile $TiO_2$. *Chem. Mater.* **2008**, *20*, 3435–3442.
48. Stankovich, S.; Dikin, D. A.; Piner, R. D.; Kohlhaas, K. A.; Kleinhammes, A.; Jia, Y.; Wu, Y.; Nguyen, S. T.; Ruoff, R. S. Synthesis of Graphene-Based Nanosheets *via* Chemical Reduction of Exfoliated Graphite Oxide. *Carbon* **2007**, *45*, 1558–1565.
49. Yamabi, S.; Imai, H. Crystal Phase Control for Titanium Dioxide Films by Direct Deposition in Aqueous Solutions. *Chem. Mater.* **2002**, *14*, 609–614.
50. Wang, D. H.; Liu, J.; Huo, Q. S.; Nie, Z. M.; Lu, W. G.; Williford, R. E.; Jiang, Y. B. Surface-Mediated Growth of Transparent, Oriented, and Well-Defined Nanocrystalline Anatase Titania Films. *J. Am. Chem. Soc.* **2006**, *128*, 13670–13671.